Stereo-PIV Experiments and Large Eddy Simulations of Flow Fields in Stirred Tanks with Rushton and Curved-Blade Turbines

Zhipeng Li, Ge Song, Yuyun Bao, and Zhengming Gao
State Key Laboratory of Chemical Resource Engineering, School of Chemical Engineering, Beijing University of Chemical Technology, Beijing 100029, China

DOI 10.1002/aic.14117
Published online September 3, 2013 in Wiley Online Library (wileyonlinelibrary.com)

The flow characteristics in pilot-scale stirred tanks with Rushton and curved-blade turbines were investigated by using stereoscopic particle image velocimetry (SPIV) experiments and large eddy simulation (LES) methods. The velocity and turbulent kinetic energy (TKE) in the impeller discharge regions were carefully resolved with a high resolution SPIV system, and the detailed phase-resolved velocity and TKE profiles were used to validate the LES results. The effects of Reynolds number and blade shape on the flow characteristics were discussed. The LES results of velocity, TKE, and the evolution of trailing vortices were compared with the SPIV experimental data, and good agreement was obtained at various phase angles. The effects of subgrid scale model and hybrid grid with different mesh resolutions on the LES results were investigated. LES is a computationally affordable method for the accurate predictions of the complex flow fields in pilot-scale stirred tanks is presented. © 2013 American Institute of Chemical Engineers *AIChE J*, 59: 3986–4003, 2013
Keywords: stereo-particle image velocimetry experiment, large eddy simulation, curved-blade turbine, stirred tank, hydrodynamics

Introduction

Stirred tank reactors equipped with curved-blade disk turbines are widely used in multiphase process industries, such as fermentation, pharmaceutical engineering, and polymerization reactions. However, compared with the numerous research on the characteristics of gas dispersion,[1–4] few studies have been conducted on the flow hydrodynamics of such stirred tanks.[5–7]

Experimental investigation is the fundamental method to reveal the flow characteristics in stirred tanks. Up to now, a large number of studies on the flow fields in stirred tanks with radial flow impellers have been carried out by using nonintrusive techniques, such as laser Doppler velocimetry (LDV) and particle image velocimetry (PIV).[8–15] For the LDV technique, it is convenient to accurately obtain the time series of velocity with high frequency and further analyze the energy spectrum of velocity. One advantage of the PIV technique is that it can conveniently be used to obtain the instantaneous velocity of a whole illuminated plane. The frequency characteristics of flow field can be measured and analyzed by using high speed or time-resolved PIV. Standard two-dimensional PIV apparatus are widely used to resolve the flow fields of stirred tanks. However, because the velocity perpendicular to the measurement plane cannot be obtained directly, a pseudo-isotropic assumption is often utilized to calculate the turbulent kinetic energy (TKE).[16] Escudie and Line measured the three velocity components, their corresponding gradients, and TKE based on two-dimensional PIV experiments carried out in multiple radial, tangential, and horizontal measurement planes.[13] Another method to calculate TKE accurately is based on stereoscopic PIV (SPIV) measurements, but such experiments are complex, time-consuming, and expensive. Therefore, few SPIV studies have been conducted to measure the radial flow field of stirred tanks with Rushton[14] and sawtooth[15] impellers, and the hydrodynamics in curved-blade stirred tanks have not been resolved by using the SPIV technique until the present work.

The flow characteristics near an impeller are typically periodic as the movement of blades, and a phase-averaged method is often recommended to obtain the mean flow patterns.[8,11,13] Phase-resolved methods are also used to reveal the dynamic flow patterns and their corresponding evolutions effected by the rotation of blades. Therefore, both phase-averaged and phase-resolved methods were used in the present stereoscopic PIV experiments.

Computational fluid dynamics (CFD) methods are now playing an important role in predicting the flow and mixing characteristics of stirred tanks. Joshi et al. [17,18] reviewed in detail the current status of the CFD simulations applied to stirred tanks, including the modeling of impeller-baffle interaction, turbulence modeling for single-phase systems with radial impellers or axial impellers, and energy transport. As an intermediate method between Reynolds averaged Navier–Stokes (RANS) and direct numerical simulation (DNS)

Correspondence concerning this article should be addressed to Z. Gao at gaozm@mail.buct.edu.cn.

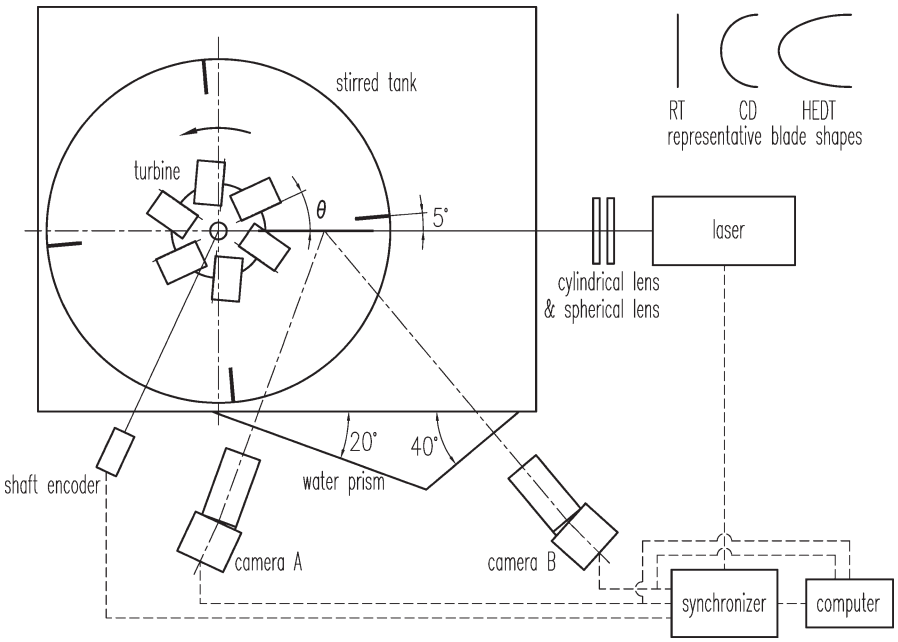

Figure 1. Experimental setup for stereoscopic PIV system.

approaches, large eddy simulation (LES) directly resolves large-scale turbulent flow structures and models small eddies by using a subgrid scale (SGS) model, thus overcoming the limitations of RANS methods, such as the underprediction of TKE and the inaccurate movement of trailing vortices, with lower computational costs than those of the DNS technique. Based on the development of high performance computing and massively parallel architectures, the LES approach is very promising for the prediction of turbulent flow systems with complex geometries.

As the first LES work on the turbulent flow in a mechanically stirred tank performed by Eggels,[19] the LES approach has gradually become a popular tool to investigate the flow characteristics of stirred tanks.[20–42] The lattice Boltzmann scheme,[20–23] finite difference method,[5,6,24,25] spectral multidomain technique,[26,27] and finite volume method[28–42] are usually used to discretize the governing equations of LES. Lu et al. tested the performance of nonuniform grid for the lattice Boltzmann scheme and found that the computation time can be reduced by 75% below that for uniform grid.[22] Several SGS models, such as the implicit model,[24] Voke model,[23] renormalization group model,[31] structure function model,[21] and standard and dynamic Smagorinsky models, were implemented in modeling the flow patterns of stirred tanks. However, for the stirred tanks with radial flow impellers, most LES studies have involved the standard Rushton turbine (RT), and only a few have used curved-blade disk turbines.[5,6]

In the present study, stereoscopic PIV measurements were conducted in pilot-scale stirred tanks with Rushton and curved-blade turbines. Both the phase-resolved and the phase-averaged velocity and TKE were carefully measured by using high resolution cameras. The effects of Reynolds number and blade shape on the flow characteristics were discussed. LESs were also performed for such stirred tanks, and the simulated results were compared with the stereoscopic PIV data. The effects of subgrid scale model and hybrid grid on the simulated results were investigated. The characteristics of the trailing vortices were also discussed.

Further to the published works in this field,[5–7] quantitative phase-resolved experimental data were provided in detail for the first time. The LES results with four SGS models were carefully verified, and good agreement between experimental and predicted results was obtained. The effects of Reynolds number and mesh resolution of hybrid grid on the phase-resolved flow characteristics were also discussed for the first time.

Experimental Setup

Stirred tank and disk turbines

The cylindrical stirred tank used in this work was a flat bottom Perspex vessel with an inner diameter $T = 0.48$ m. Four baffles each with a width of $10/T$ and thickness of 0.01 m were equally spaced in the tank. A plane 5° behind a baffle was chosen as the measurement plane to avoid the refraction of the edges of the baffles, as shown in Figure 1. The working fluid was tap water and the liquid height H was equal to T. The kinematic viscosity of the tap water v was 10^{-6} m^2/s. The cylindrical stirred tank was placed in a cuboid-shaped tank filled with tap water to minimize the refraction of the laser sheet. A water prism was used to keep the axes of the two camera lenses perpendicular to the corresponding water–air interfaces.

The three disk turbines used were a RT, half circular blades disk turbine (CD), and half elliptical blades disk turbine (HEDT). The profiles of the blades are schematically shown in the top right corner of Figure 1, and the solid models of the three disk turbines are shown in Figure 2. The diameter D was 0.19 m and the impeller clearance from the bottom of the tank was 0.158 m for each disk turbine. The diameter and thickness of each of the three disks were 0.13 and 0.004 m, respectively, and the length, width, and thickness of each blade were 0.06, 0.038, and 0.002 m, respectively.

Five rotational speeds of the three disk turbines, $N = 66.5$, 83.1, 99.7, 124.7, and 149.6 rpm, were chosen, and the corresponding Reynolds numbers, $\mathrm{Re} = ND^2/v$, were 40,000,

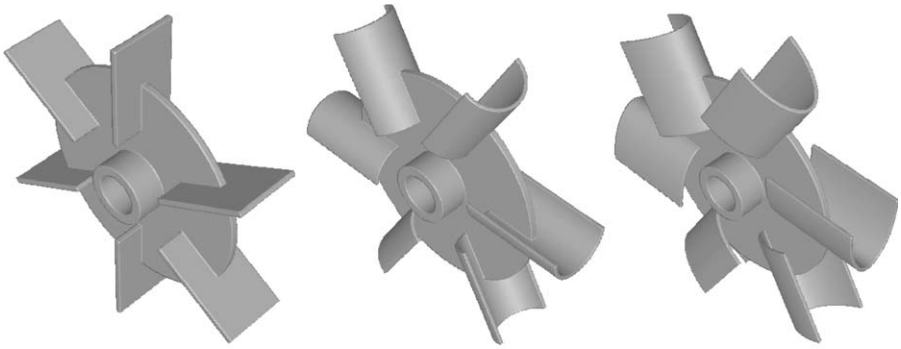

Figure 2. Turbine geometries.

(a) RT; (b) CD; and (c) HEDT.

50,000, 60,000, 75,000, and 90,000, respectively. These operating conditions were used to investigate the influence of Reynolds number on the flow phenomena in the stirred tanks. The turbines were driven by a motor (ABB), and the rotational speeds were controlled by a frequency converter (Danfoss, Denmark).

SPIV technique

A stereoscopic PIV system (TSI) was used for the measurements of the flow fields. The laser sheet illuminating the measurement plane was generated by a dual pulsed laser system (New Wave Research Solo, Nd:YAG, 532 nm, 200 mJ, 15 Hz) and converted by spherical and cylindrical lenses. The particles used to seed the flow were 10 μm hollow spherical glass particles with nearly neutral buoyancy in water. Two frame-straddling CCD cameras (PowerView Plus, 4008 × 2672 pixels) with lenses (Micro Nikkor 60 mm, Nikon, Japan) were used to capture the particle displacement. Asymmetric SPIV arrangement[43] was utilized, and the lenses and the cameras were mounted on an electromechanical translation apparatus to satisfy the Scheimpflug condition, which requires the measurement, image, and lens principle planes to intersect at a common point, as shown in Figure 1.

The phase angle between the current (or measured) blade and the measurement plane is denoted by θ, as shown in Figure 1. An encoder (Kubler, Germany) was used to locate the specific phase angles required by the phase-resolved SPIV measurements. Transistor–transistor logic (TTL) signals triggered by the encoder were used by a synchronizer (TSI) to synchronize image acquisition and laser firing. For each turbine, the SPIV experiments were conducted at 30 different phase angles; that is, the phase-resolved measurements were obtained every 2° behind the current blade.

Calibration was conducted in the region near the disk turbine by using a one-sided, two-layer rectangular black calibration target. White 1-mm diameter calibration markers were equally distributed on the target to form a calibration grid, and a fiducial mark cross was located in the center of the target. The final field of view was the overlap region focused by the two cameras and was about 0.1 m × 0.1 m. The Insight 3G software was used to cross-correlate the images on 32 × 32 pixels interrogation windows with 50% overlap, and a stereo automapping algorithm was used to correct the misalignment error between the calibration target and the laser sheet. The spatial resolution of the velocity vectors was about 0.8 mm. The time interval between a pair of images was evaluated by examining the displacements of illuminated particles and optimized to ensure that the maximum in-plane and out-of-plane displacements of seeding particles were less than one-quarter of the interrogation spot size and the thickness of laser sheet. Therefore, a time interval of 200 μs was set for $N = 66.5$ rpm, 150 μs for $N = 83.1$ and 99.7 rpm, and 100 μs for $N = 124.7$ and 149.6 rpm.

The statistical convergence was verified on the mean velocity, fluctuating velocity, and TKE, and the difference between the fluctuating velocities calculated from 300 and 400 pairs of images was smaller than 1.5%. Thus, 400 pairs of images were captured at each phase behind the blade to obtain the phase-resolved results, and the phase-averaged data were calculated from the 30 phase-resolved results for each turbine.

Large Eddy Simulation

Subgrid scale model

The basic governing equations of LES for incompressible flows are the filtered continuity and Navier–Stokes equations

$$\frac{\partial \bar{u}_i}{\partial x_i} = 0 \tag{1}$$

$$\frac{\partial \bar{u}_i}{\partial t} + \frac{\partial \bar{u}_i \bar{u}_j}{\partial x_j} = -\frac{1}{\rho}\frac{\partial \bar{p}}{\partial x_i} + \nu \frac{\partial^2 \bar{u}_i}{\partial x_j \partial x_j} - \frac{\partial \tau_{ij}}{\partial x_j} \tag{2}$$

where the overbars denote the resolvable scales obtained from grid filtering. The effect of subgrid scales appears through the subgrid scale stress tensor, which must be modeled

$$\tau_{ij} = \overline{u_i u_j} - \bar{u}_i \bar{u}_j \tag{3}$$

In the present work, four SGS models, namely the standard Smagorinsky–Lilly model (SSL), the dynamic Smagorinsky–Lilly model (DSL), the dynamic kinetic energy (DKE) model, and the wall-adapting local eddy (WALE) viscosity model, were used to model the interaction between the resolved scales and the unresolved scales of the flow. These models are all eddy viscosity models, and the unknown subgrid scale stress tensor τ_{ij} and the filtered rate of strain tensor $\bar{S}_{ij}$ are related by

$$\tau_{ij} - \frac{1}{3}\delta_{ij}\tau_{kk} = -2\nu_t \bar{S}_{ij} \tag{4}$$

The SSL model is based on the work of Smagorinsky,[44] and the eddy viscosity is modeled as[45]

$$v_t = (\min(\kappa d, C_S\Delta))^2 |\bar{S}| \quad (5)$$

where κ is the von Karman constant, d is the distance to the closest wall, C_S is the Smagorinsky coefficient and was set as 0.1 in this work, Δ is the filter width, and $|\bar{S}|$ is the modulus of strain rate for the resolved scales.

Because no universal Smagorinsky coefficient is suitable for different flow fields, Germano et al.[46] and Lilly[47] conceived an approach to dynamically compute the Smagorinsky coefficient from the information of resolved scales.

In the DSL model, a second "test" filter (denoted by a tilde) to the large eddy governing equation is required, and the subgrid scale stress in the test filter is expressed as follows

$$T_{ij} = \widetilde{u_i u_j} - \widetilde{\bar{u}_i}\,\widetilde{\bar{u}_j} \quad (6)$$

T_{ij}, which is similar to τ_{ij}, is associated with large scales

$$T_{ij} - \frac{1}{3}\delta_{ij}T_{kk} = -2\left(C_s\tilde{\Delta}\right)^2 |\widetilde{\bar{S}}|\,\widetilde{\bar{S}_{ij}} \quad (7)$$

The stresses T_{ij} and τ_{ij} are related as follows

$$L_{ij} \equiv T_{ij} - \tilde{\tau}_{ij} \quad (8)$$

where L_{ij} is the stress associated with the small-resolved scales between the test and grid filters. Thus, Eqs. 4, 7, and 8 can be combined into

$$L_{ij} - \frac{1}{3}\delta_{ij}L_{kk} = C_S^2 M_{ij} \quad (9)$$

where

$$M_{ij} = -2\tilde{\Delta}^2 |\widetilde{\bar{S}}|\,\widetilde{\bar{S}_{ij}} + 2\Delta^2 \widetilde{|\bar{S}|\bar{S}_{ij}} \quad (10)$$

The model coefficient is calculated as

$$C_S^2 = \frac{L_{ij}M_{ij}}{M_{ij}M_{ij}} \quad (11)$$

The DKE model proposed by Kim and Menon[48] accounts for the history and nonlocal effects by solving the transport equation of subgrid scale TKE k_{sgs}

$$\frac{\partial k_{\text{sgs}}}{\partial t} + \bar{u}_i\frac{\partial k_{\text{sgs}}}{\partial x_i} = -\tau_{ij}\frac{\partial \bar{u}_i}{\partial x_j} - C_\varepsilon\frac{k_{\text{sgs}}^{3/2}}{\Delta} + \frac{\partial}{\partial x_i}\left(v_t\frac{\partial k_{\text{sgs}}}{\partial x_i}\right) \quad (12)$$

The subgrid scale eddy viscosity is computed as follows

$$v_t = C_k k_{\text{sgs}}^{1/2}\Delta \quad (13)$$

where the model constants C_k and C_ε are determined dynamically.[48]

The WALE model[49] was designed to obtain correct wall behavior for wall-bounded flows, and the eddy viscosity is modeled by

$$v_t = (\min(\kappa d, C_w\Delta))^2 \frac{\left(S_{ij}^d S_{ij}^d\right)^{3/2}}{\left(\bar{S}_{ij}\bar{S}_{ij}\right)^{5/2} + \left(S_{ij}^d S_{ij}^d\right)^{5/4}} \quad (14)$$

where

$$S_{ij}^d = \frac{1}{2}\left(\bar{g}_{ij}^2 + \bar{g}_{ji}^2\right) - \frac{1}{3}\delta_{ij}\bar{g}_{kk}^2,\ \bar{g}_{ij} = \frac{\partial \bar{u}_i}{\partial x_j} \quad (15)$$

Numerical method

The geometric parameters used for the LES models in this work were the same as those described in the section on experimental setup. Based on our previous LES studies using totally hexahedral cells,[39–41] a slightly finer grid consisting of approximately two million unstructured, nonuniformly distributed hexahedral cells was used for the current LESs of stirred tank with RT impeller. The impeller discharge region was discretized by finer cells than those used in other regions of the tank, and the averaged cell sizes in these two regions were about 1.5 and 4 mm, respectively. As for the LES of stirred tanks with CD and HEDT impellers, hybrid grids including tetrahedral, pyramidal, and hexahedral cells were used. The effect of hybrid grids with different mesh resolutions, including a coarse grid with about three million cells, a medium grid with about six million cells, and a fine grid with about 10 million cells, on the flow field was investigated. Homogeneous refinement among the three hybrid grids was used to keep a similar grid topology in each grid.

The numerical simulations were conducted using the commercial software package ANSYS FLUENT 13, which is based on the finite volume method of unstructured grids. The linear equations were solved by using an algebraic multigrid procedure. The impeller movement was modeled by using the sliding mesh model for unstructured grids. The center differencing scheme was used for the spatial discretization of the momentum equations, and the second-order accurate implicit scheme for time advancement. The coupling between the continuity and momentum equations was achieved by using the pressure implicit with splitting of operators algorithm.

Steady state $k-\varepsilon$ calculations were utilized for all LES cases to provide good initial values for the transient LESs. The condition of no-slip velocity was applied to all solid wall boundaries. The free surface of the tank was considered as a symmetry boundary.

During one impeller revolution, 720 time steps were used for the case with fine hybrid grids, and 360 time steps were used for all the other cases. To ensure that every normalized residual dropped below the specified convergence tolerance (10^{-4}), 30 iterations per time step were required for all cases. The velocities and impeller torques were also monitored during the calculations. The LES results could reach quasi-steady state after about 20 revolutions, and then the flow data were collected and statistically processed in the subsequent 20 revolutions for the case with fine hybrid grids and 40 revolutions for all the other cases. Because gathering data for time statistics inside a sliding zone is not meaningful in the commercial code ANSYS FLUENT,[45] a user-defined subroutine was used for the LES postprocessing in the present work. In the subroutine, the instantaneous velocity fields in absolute Cartesian coordinates were collected at specified time steps and phase angles and statistically processed at the end of the simulation, and then the results were exported. In our LESs, the calculated TKE includes contributions from both resolved and modeled scales, but the SGS contribution is less than 1% of the total TKE at all phase angles.

The above-mentioned simulations were performed on an eight-node cluster, and each node consisted of two six-core Intel Xeon processors, 24 GB memory, and a Red Hat Linux operating system.

Results and Discussion

In the following discussion of SPIV and CFD results, the radial, axial, and tangential mean velocities are represented by U, V, and W, respectively, and the velocities are normalized with the impeller tip velocity V_{tip}. The TKE is represented by k and normalized with V_{tip}^2. The origin of the coordinates is located at the center of the disk of the turbine. The axial coordinate is normalized with the half width of the blade $w/2$ and denoted by $2z/w$, and the radial coordinate is normalized with the radius of the turbine R and denoted by r/R.

Effect of Reynolds number on flow characteristics

Different scale-up criteria, such as constant power per unit volume, constant impeller tip velocity, and constant mixing time, are commonly used for the design and optimization of stirred tanks. Fully obtaining the flow characteristics under various operating conditions determined by different scale-up methods is impractical and not necessary. For a given stirred tank with given impellers, different scale-up methods induce different operating speeds or Reynolds numbers, so the effect of Reynolds number on the turbulent hydrodynamics of stirred tank is considered here.

Phase-resolved SPIV measurements were conducted for RT, CD, and HEDT impellers with Reynolds number ranging from 40,000 to 90,000, and the results for the RT impeller at $\theta = 20^\circ$ are presented in Figure 3. The normalized profiles of the radial velocity at different Reynolds numbers almost collapse onto one line, as shown in Figures 3a, b, and only slight differences can be observed near the peak values. The profiles of the axial velocity, tangential velocity, and TKE further confirm the similarity of different Re cases. Similar results on the normalized velocity and turbulence profiles of CD and HEDT impellers were obtained but not presented here for conciseness. Therefore, the Reynolds number has almost no influence on the normalized phase-resolved velocity and TKE profiles under the present experimental conditions.

On the basis of the results of the phase-resolved flow fields, it can be concluded that the normalized phase-averaged flow characteristics are independent of the Reynolds number for the fully turbulent flow in baffled stirred tanks with CD and HEDT impellers, and this similarity has been experimentally validated in stirred tanks with Rushton impeller by several researchers.[10,14,40] However, in unbaffled stirred tanks, the phase-averaged flow patterns vary with the Reynolds number ranging from 4000 to 64,000,[27] and this characteristic must be taken into account during the design and scale-up of such stirred tanks.

Effect of blade shape on phase-averaged flow field

Phase-averaged velocity and TKE distributions are useful for the application of stirred tanks in process engineering. The left column of Figure 4 shows the normalized phase-averaged results for RT, CD, and HEDT impellers at the same Reynolds number of 50,000. The typical radial discharge streams of these turbines can be clearly observed from the vectors and streamlines. However, the slightly upward characteristic of the discharge stream of RT impeller (Figure 4a) is not as evident as those reported in the literature,[8,9,13] probably because of the minor differences of the RTs used. That is, a modified RT with a smaller disk diameter of 0.68 D and longer blade length of 0.32 D was used in the present work, while standard RTs with a disk diameter of 0.75 D and blade length of 0.25 D are usually reported in the literature. Another reason may be the positions of the measurement planes. A plane 5° behind a baffle was used in this study, while one in the middle of two successive baffles was often used by previous investigators. When the blades are streamlined, as shown in Figures 4b, c, the discharge streams become flatter.

The contours in Figures 4a–c illustrate the distributions of TKE, but the regions with k/V_{tip}^2 less than 0.02 are not presented for conciseness. Depending on the characteristics of the discharge streams, the slightly upward trends gradually decrease in the order of RT, CD, and HEDT. The high phase-averaged TKE regions are mainly located in the discharge regions for all three turbines and evidently decrease with the spread of the streams. The different maximum TKE levels for RT, CD, and HEDT impellers at the same Reynolds number are attributed to the different power consumptions. The measured ungassed power numbers for RT, CD, and HEDT are 5.3, 3.1, and 2.2, respectively.

Using the results of the above section, the absolute velocity and TKE distributions for RT, CD, and HEDT at the same power consumption ($P = 3.5$ W) were obtained and are shown in Figures 4d–f. The corresponding tip velocities for RT, CD, and HEDT are 0.83, 0.99, and 1.1 m/s, respectively. When the power consumptions of these impellers are equal, both the distributions of different TKE levels and the region of each level are very similar for these impellers. For example, the TKE levels for the three turbines all range from 0.02 to 0.07 $m^2\ s^{-2}$ (see Figures 4d–f), and the shapes of the TKE contours are similar at TKE levels lower than 0.06 $m^2\ s^{-2}$. Previous studies showed that blade streamlining could improve the gas dispersion in stirred tanks,[1–4] but the gas dispersion characteristics of these turbines are not included in this paper and will be investigated in the future. The focus of the present study is to present detailed velocity and TKE distributions for curved-blade turbines under ungassed conditions.

Comparison of four SGS models

To evaluate the performance of SGS models, phase-resolved LES results with four SGS models are compared with stereoscopic PIV data, and the velocity and TKE profiles are shown in Figures 5–8. The standard deviations of the differences between the above experimental and simulated profiles are listed in Table 1. The comparisons are based on the flow field of the RT impeller, and only the results at three phase angles are listed for conciseness. The fully hexahedral grid, the boundary conditions, the discretization schemes, and the statistical method are all the same, but the SGS model is different in each LES. The vertical coordinates of each figure are not restricted to the same scale so as to enlarge the graphics and obtain clear comparison of the results.

Figures 5–8 show that, in general, the phase-resolved LES results with four different SGS models are in good agreement with the SPIV experimental data, although there are some discrepancies. The LES results with the WALE model give the best estimation of radial velocity at $2z/w = 1.0$, as shown in Figures 5d–f and Table 1, while the predictions of radial velocity at $2z/w = 0$ and $r/R > 1.2$ deviate significantly from the SPIV data (see Figures 5a–c and Table 1). Good and bad agreement presented by this model can also be observed simultaneously in the predictions of axial and tangential velocities (see Figures 6, 7 and Table 1). In Figure 8,

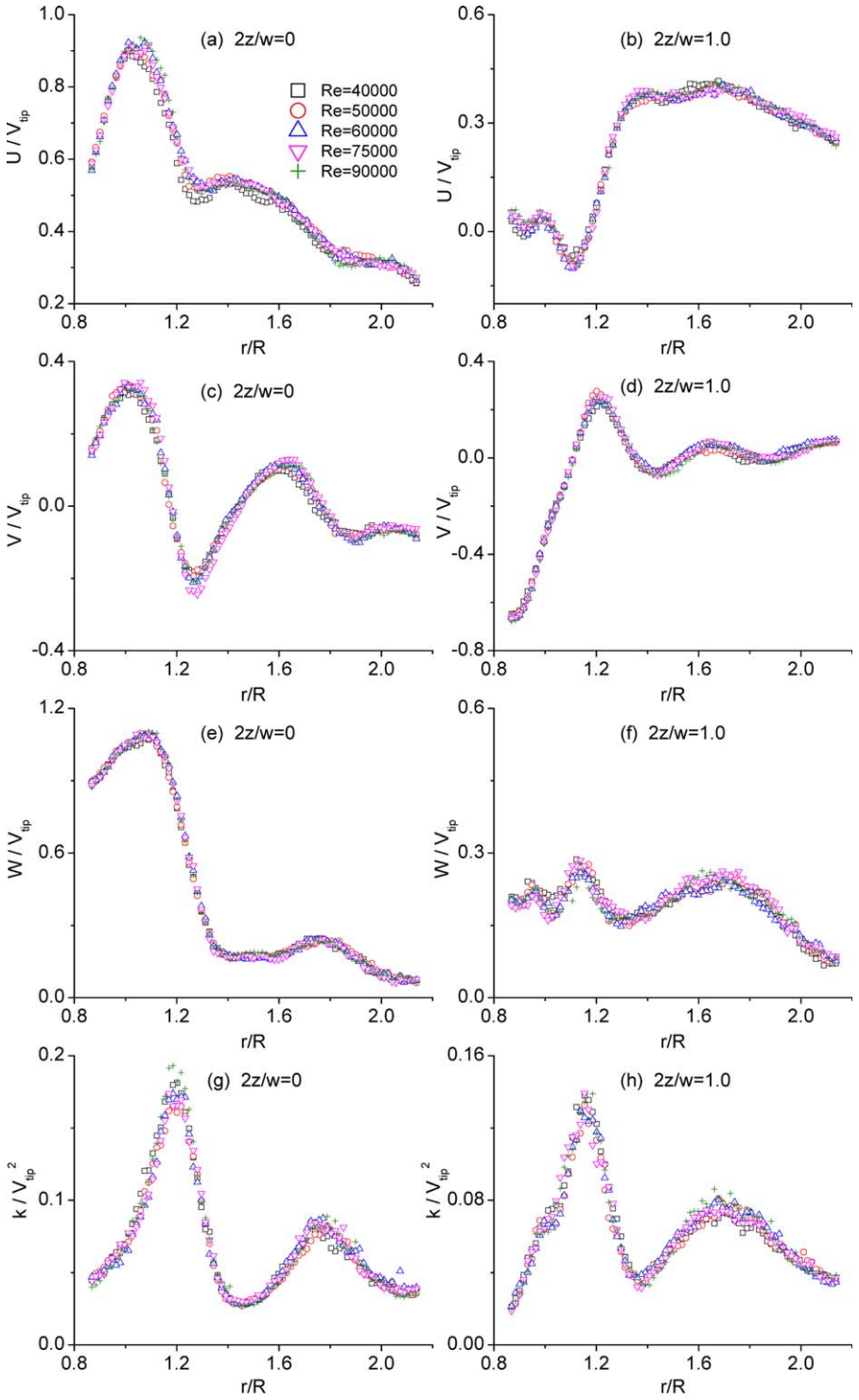

Figure 3. Phase-resolved velocity and TKE profiles obtained by SPIV for RT impeller at $\theta = 20°$.

[Color figure can be viewed in the online issue, which is available at wileyonlinelibrary.com.]

the LES results with the WALE model agree well with the SPIV data except for some local deviations (see Figures 8c, d), and the WALE model gives the smallest averaged standard deviation of the TKE difference of the four SGS models, as listed in Table 1. Therefore, the WALE SGS model appears to be promising for the simulation of stirred tanks, probably because of the consideration of the effects of smallest resolved turbulent fluctuations.[49] However, because very few LES studies based on the WALE model have been conducted in quantitatively predicting the flow fields of stirred tanks until the present study, the WALE model needs to be further verified, and the above-mentioned unsteady behavior of the simulated results should be further investigated.

The DKE model presents obvious discrepancies in the predictions of radial velocity (see Figure 5), tangential velocity (see Figures 7c, f), and TKE (see Figure 8) and gives the largest averaged standard deviations for both mean velocity components and TKE, although the SGS turbulence may be better modeled by accounting for the transport of the SGS TKE in this model.[48]

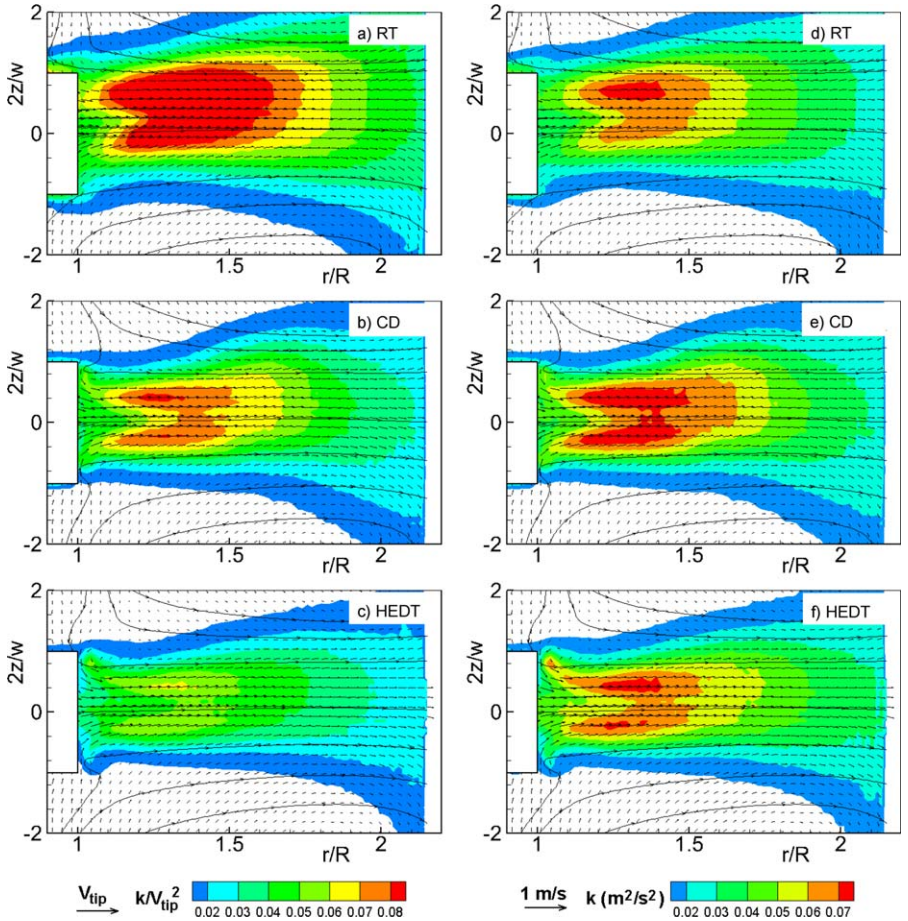

Figure 4. Phase-averaged velocity and TKE fields obtained by SPIV.

Left column: at constant Reynolds number, Re = 50,000; Right column: at constant power consumption, $P = 3.5$ W. [Color figure can be viewed in the online issue, which is available at wileyonlinelibrary.com.]

The agreement between the predictions of the SSL and DSL models and the SPIV data varies for different velocity and TKE profiles, as shown in Figure 5–8 and Table 1. In terms of averaged standard deviation (see Table 1), the SSL model gives lower values for the radial and tangential velocity profiles, a higher value for the axial velocity profile, and the same value for the TKE profile in comparison with the DSL model. In other words, the SSL model presents slightly better predictions than the DSL model in the present study, but the difference is not significant. Considering the

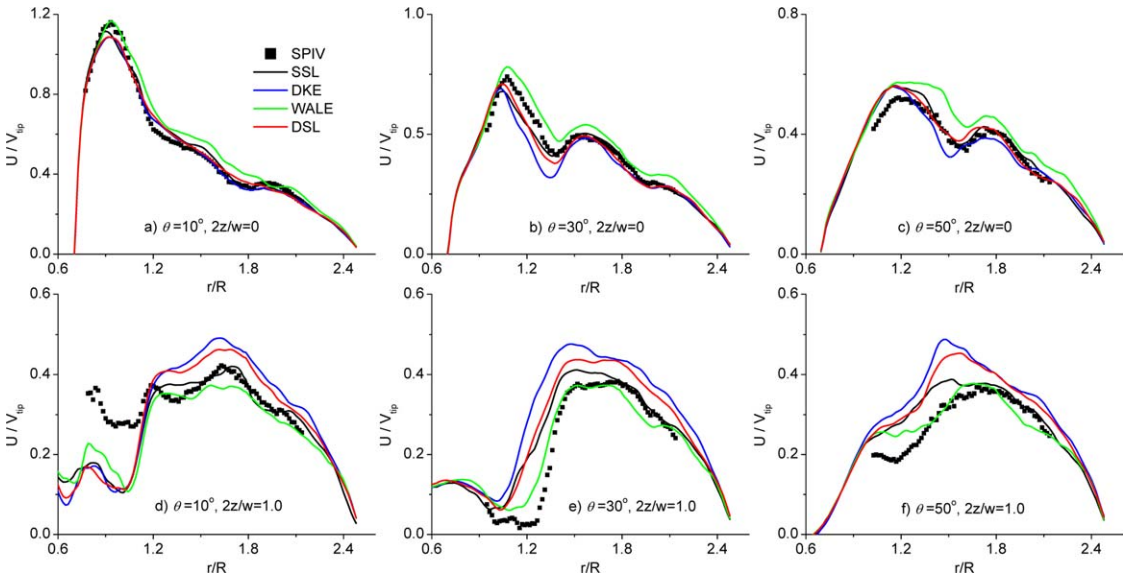

Figure 5. Phase-resolved radial velocity profiles for RT impeller using SPIV and LES with four SGS models.

[Color figure can be viewed in the online issue, which is available at wileyonlinelibrary.com.]

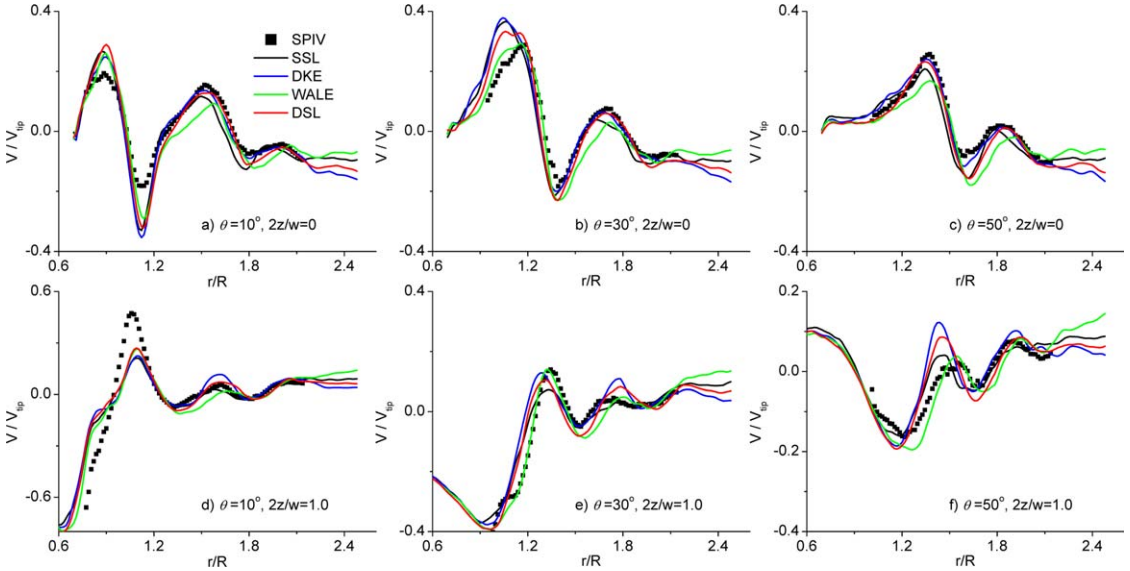

Figure 6. Phase-resolved axial velocity profiles for RT impeller using SPIV and LES with four SGS models.

[Color figure can be viewed in the online issue, which is available at wileyonlinelibrary.com.]

principles of the SSL and DSL models, the DSL model was chosen for the LES calculations of stirred tanks with CD and HEDT impellers in the present work.

The general agreement between the phase-resolved LES results with different SGS models and the SPIV data can further confirm the accuracy of phase-averaged LES predictions. Phase-averaged LES results with the structure function model and Smagorinsky model were quantitatively compared by Derksen,[21] and those with the Voke SGS model and Smagorinsky model were assessed by Hartmann et al.[23] In both investigations, good agreement between the SGS models has been reported. The flow fields in stirred tanks are usually periodic as the rotation of the impeller, so phase-resolved results can present more details than phase-averaged data and should be used to evaluate the performance of different SGS models. For example, the radial velocity is underestimated at $2z/w = 1.0$ and $r/R = 1.0$ (see Figure 5d), but overestimated at the other two phase angles (see Figures 5e, f). If the phase-averaged method is adopted, the positive and negative deviations at different phase angles will cancel out each other, and the total deviation may be decreased or even eliminated.

Influence of hybrid grid on phase-resolved flow field

Our previous work showed that LES with fully hexahedral cells can benefit from the refinement of grid.[40] However, for the simulations of stirred tanks with curved-blade disk turbines, discretizing the domain with high-quality fully hexahedral cells are usually difficult, so hybrid grids consisting of tetrahedral, pyramidal, and hexahedral cells are often recommended. Moreover, the influence of hybrid grids with different mesh resolutions on the LES results for stirred tanks has not been reported until the present work.

Phase-resolved velocity and TKE profiles obtained by LES with three grid resolutions are quantitatively compared with the SPIV data in Figure 9, where LESs with coarse,

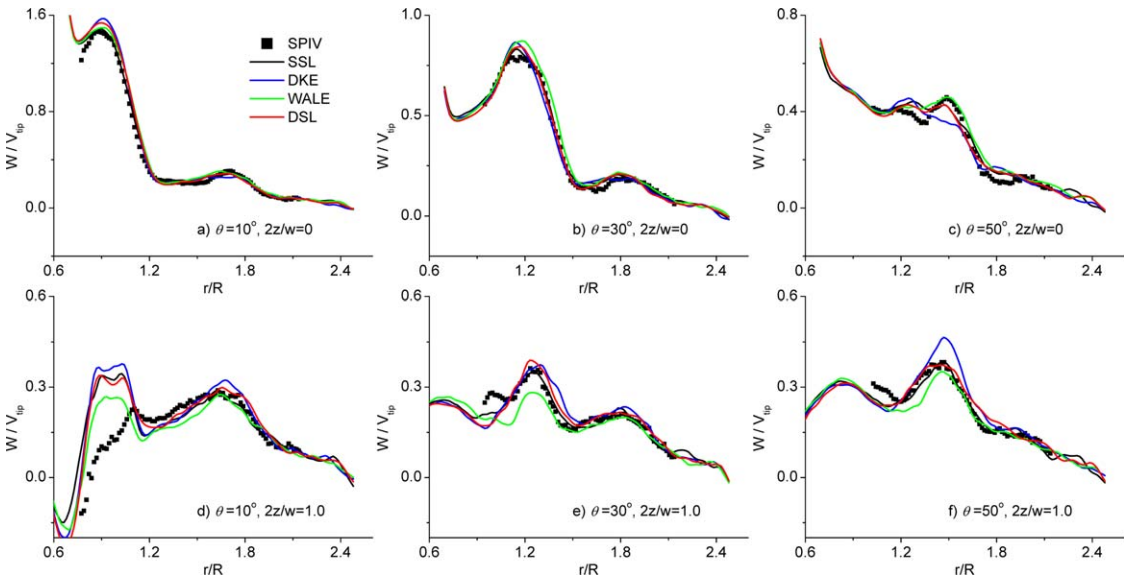

Figure 7. Phase-resolved tangential velocity profiles for RT impeller using SPIV and LES with four SGS models.

[Color figure can be viewed in the online issue, which is available at wileyonlinelibrary.com.]

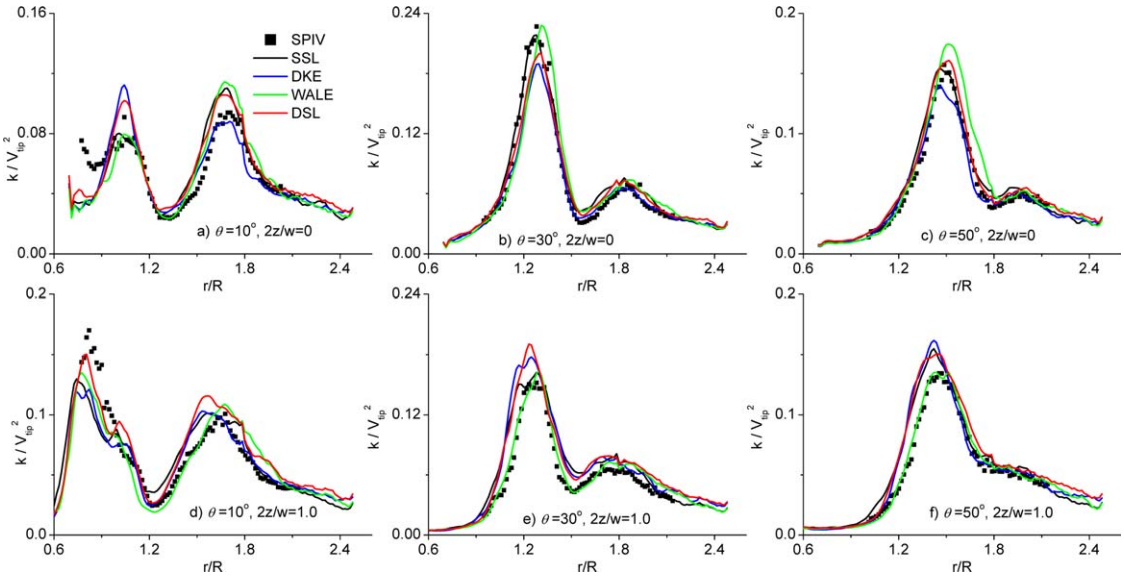

Figure 8. Phase-resolved turbulent kinetic energy profiles for RT impeller using SPIV and LES with four SGS models.

[Color figure can be viewed in the online issue, which is available at wileyonlinelibrary.com.]

medium, and fine grids are denoted by LES with coarse grid (LES CG), LES with medium grid (LES MG), and LES with fine grid (LES FG), respectively, and only the results for the CD impeller at $\theta = 0°$ are presented for conciseness.

The LES results with fine grid give the best agreement with the SPIV data, especially in the prediction of tangential velocity (Figure 9i) and TKE (Figures 9j–l). Some local oscillations may be ascribed to the insufficient statistical averaging. Because the computational resources required by LES FG are huge, the instantaneous results in the subsequent 20 revolutions were collected and averaged after reaching quasi-steady state.

The profiles simulated by LES CG and LES MG show similar shapes and distributions, and the results of LES MG are in better agreement with the experimental data than those of LES CG. The TKE values generated by both the current (or measured) blade (Figures 9k, l) and the leading blade (Figure 9l) are obviously underestimated by LES CG. Other disagreement produced by LES CG can be clearly observed in the velocity profiles shown in Figures 9a, d, i. Therefore, LES with medium grid can be considered as a reasonable method based on a compromise between computational effort and numerical accuracy, and the results obtained by this method are discussed below.

Phase-resolved results of CD impeller

Figure 10 shows the phase-resolved plots of velocity and TKE fields obtained by SPIV for the CD impeller at six-phase angles, and the corresponding LES results are illustrated in Figure 11. The velocity and TKE profiles predicted by LES at $\theta = 10°$, 30°, and 50° are quantitatively compared with the SPIV results in Figure 12, where LA, LB, and LC denote the horizontal lines at $2z/w = 0$, $2z/w = 0.5$, and $2z/w = 1.0$, respectively. These lines were chosen because they spread across the regions influenced by the trailing vortices of both the current and the leading blade. Figures 9 and 12 show the phase-resolved SPIV experimental results in the impeller discharge regions for the validation of numerical simulations of such stirred tanks.

The generation and the subsequent transport of the trailing vortices of CD impeller were resolved in detail by the SPIV experiments (see vector distributions in Figure 10), and they were successfully simulated by the LES method, as shown in Figure 11. The quantitative comparisons between the LES and SPIV results at different values of $2z/w$ (see Figure 12) further confirm the agreement. At the early stage (i.e., $\theta = 0°$ and 10°) of the transport of trailing vortices, the LES method can accurately simulate the radial, axial, and tangential velocity profiles in the region $r/R < 1.4$ (see Figures 9a–i, 12a, d, g). As the phase angle increases, some discrepancies can be observed between the experimental and predicted velocity profiles, especially the axial velocity profiles (see Figures 12c, f, i). This disagreement may be the result of using a

Table 1. Standard Deviations of Differences Between Experimental and Simulated Profiles Shown in Figures 5–8

	θ (°)	$2z/w$	SSL	DKE	WALE	DSL
U/V_{tip}	10	0	0.034	0.030	0.060	0.033
		1	0.080	0.098	0.072	0.092
	30	0	0.037	0.071	0.051	0.040
		1	0.079	0.141	0.039	0.096
	50	0	0.032	0.035	0.068	0.030
		1	0.055	0.102	0.034	0.079
	Average		0.053	0.080	0.054	0.062
V/V_{tip}	10	0	0.056	0.051	0.052	0.050
		1	0.108	0.118	0.100	0.106
	30	0	0.071	0.066	0.044	0.054
		1	0.045	0.064	0.031	0.052
	50	0	0.043	0.020	0.057	0.033
		1	0.032	0.054	0.032	0.044
	Average		0.059	0.062	0.053	0.057
W/V_{tip}	10	0	0.032	0.064	0.056	0.058
		1	0.105	0.115	0.074	0.097
	30	0	0.021	0.034	0.047	0.025
		1	0.023	0.042	0.044	0.035
	50	0	0.043	0.020	0.057	0.033
		1	0.032	0.054	0.032	0.044
	Average		0.043	0.055	0.052	0.049
k/V_{tip}^2	10	0	0.013	0.013	0.013	0.013
		1	0.019	0.018	0.016	0.017
	30	0	0.010	0.015	0.019	0.012
		1	0.021	0.025	0.009	0.022
	50	0	0.010	0.008	0.017	0.009
		1	0.016	0.018	0.005	0.017
	Average		0.015	0.016	0.013	0.015

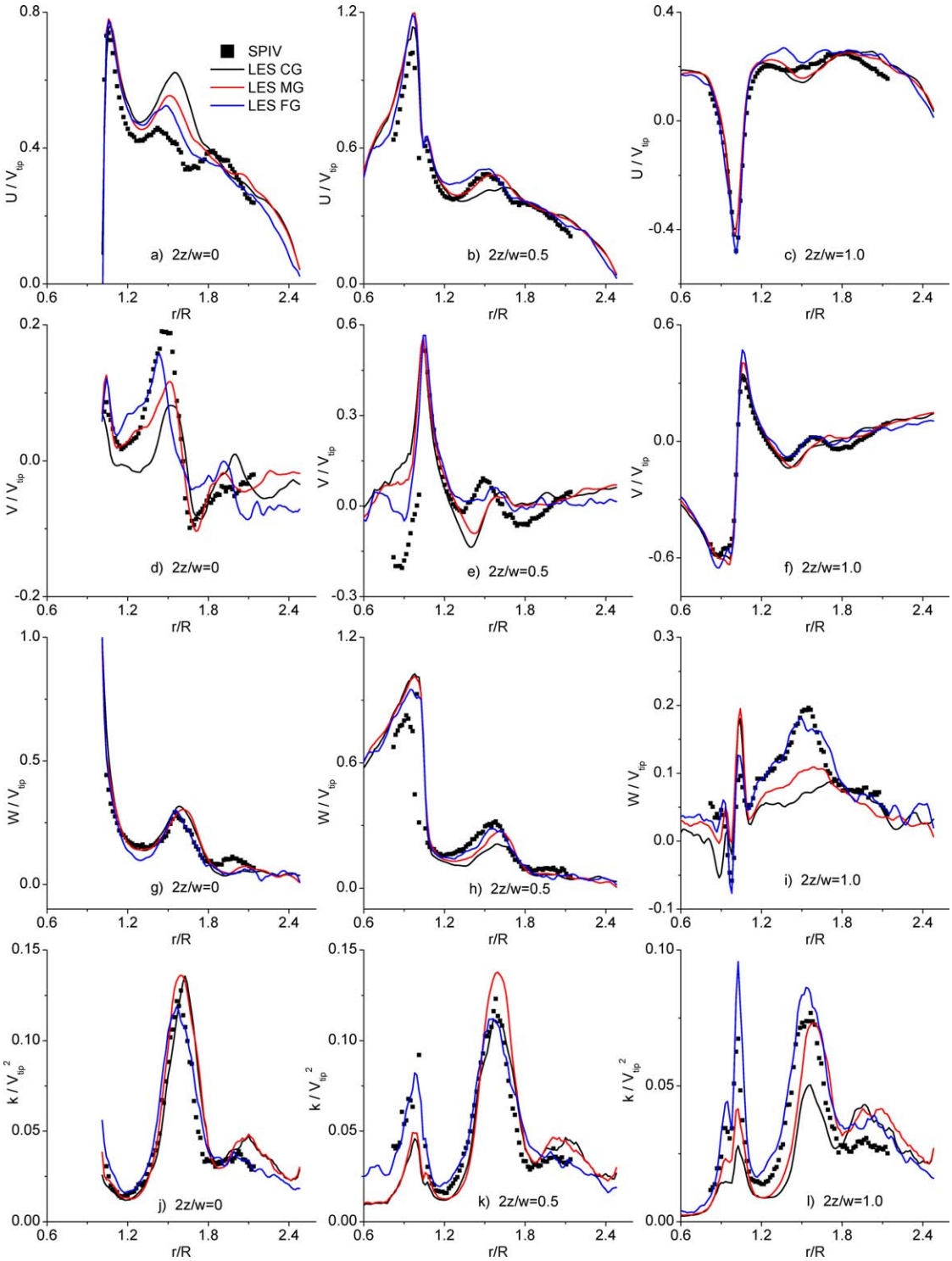

Figure 9. Phase-resolved velocity and TKE profiles obtained by SPIV and LES with coarse, medium, and fine hybrid grids for CD impeller at $\theta = 0^\circ$.

[Color figure can be viewed in the online issue, which is available at wileyonlinelibrary.com.]

hybrid grid with medium resolution. Figures 9a–i clearly show that the velocity profiles are well predicted by LES with fine grid in the region $r/R = 1.4$–1.8. This region is affected by the trailing vortices of the leading blade and is better resolved by LES FG than by LES MG.

The contours in Figures 10 and 11 show the distributions of TKE at different phase angles. The transport of phase-resolved TKE is consistent with the movement of the trailing vortices, which results in the mechanical energy transfer from the turbine to the bulk of the tank. The TKE transport process can be well predicted by using the LES method, and the simulated contour distributions are in good agreement with the SPIV results. The comparisons between the LES and SPIV data given in Figures 12j–l show that LES results can give reasonable estimations of the TKE in the impeller discharge region, where RANS-based models invariably underestimate the TKE values.[17,18] Similar to the prediction of velocity profiles, some discrepancies between the

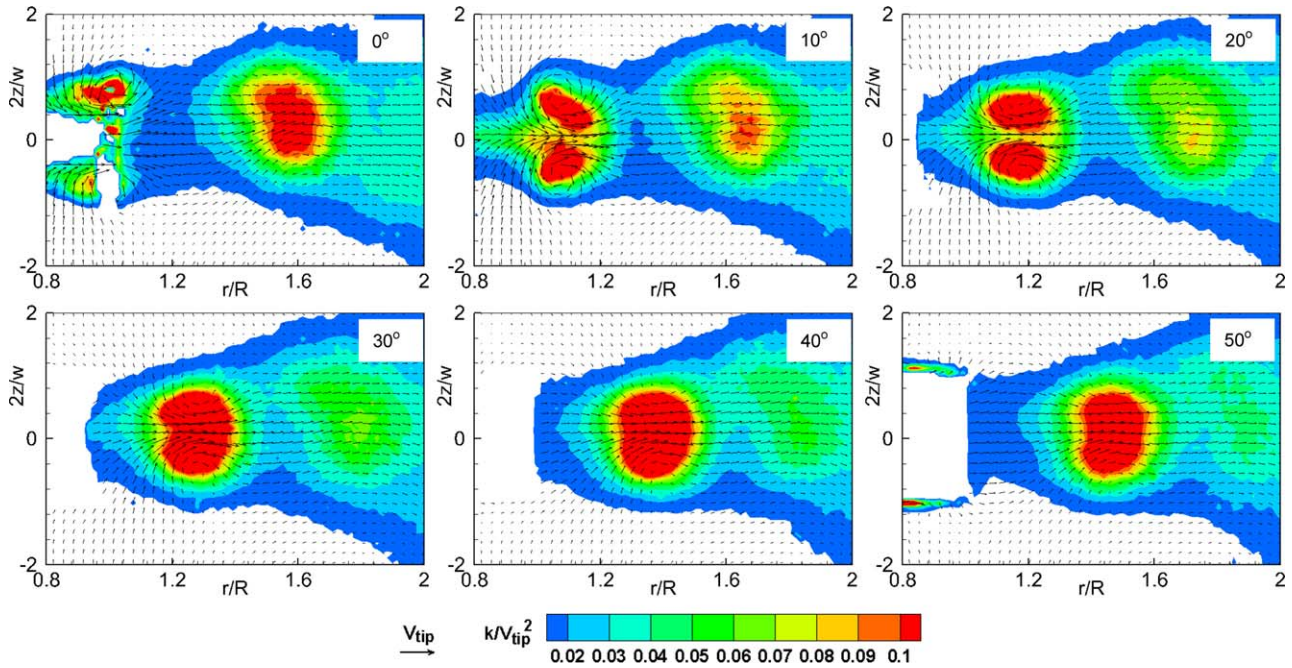

Figure 10. Phase-resolved plots of velocity and TKE fields obtained by SPIV for CD impeller at $\theta = 0°$, 10°, 20°, 30°, 40°, and 50°.

[Color figure can be viewed in the online issue, which is available at wileyonlinelibrary.com.]

experimental and predicted TKE profiles can be identified in the region affected by the trailing vortices of the leading blades, as shown in Figures 9j–l. These discrepancies may be ascribed to the insufficient grid resolution in predicting the TKE.

The overestimation of the TKE profiles has been reported by Yeoh et al.[30] and Hartmann et al.[23] for the flow fields in stirred tanks with RTs. However, it is difficult to explain the TKE overestimation in some regions (see Figures 9j–l, 12j–l) when the LES methods with medium and coarse grid are used. One possible reason is that the grid resolution used by LES has great influence on the transport of trailing vortices and TKE, and insufficient spatial resolution may cause their incorrect distributions and transport. For example, low spatial resolution can lead to underprediction of the convergence of streams in stirred tanks with dual RTs, and the underpredicted convergence further causes some overestimation of the TKE profiles in radial positions.[41]

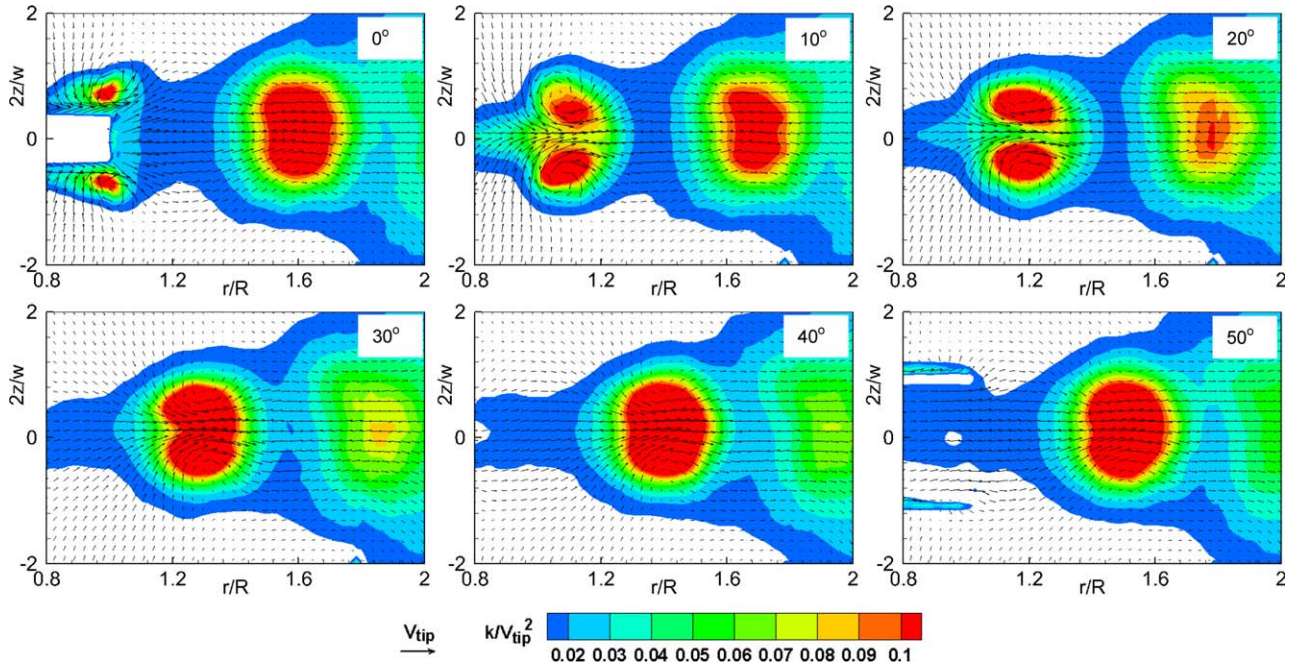

Figure 11. Phase-resolved plots of velocity and TKE fields simulated by LES for CD impeller at $\theta = 0°$, 10°, 20°, 30°, 40°, and 50°.

[Color figure can be viewed in the online issue, which is available at wileyonlinelibrary.com.]

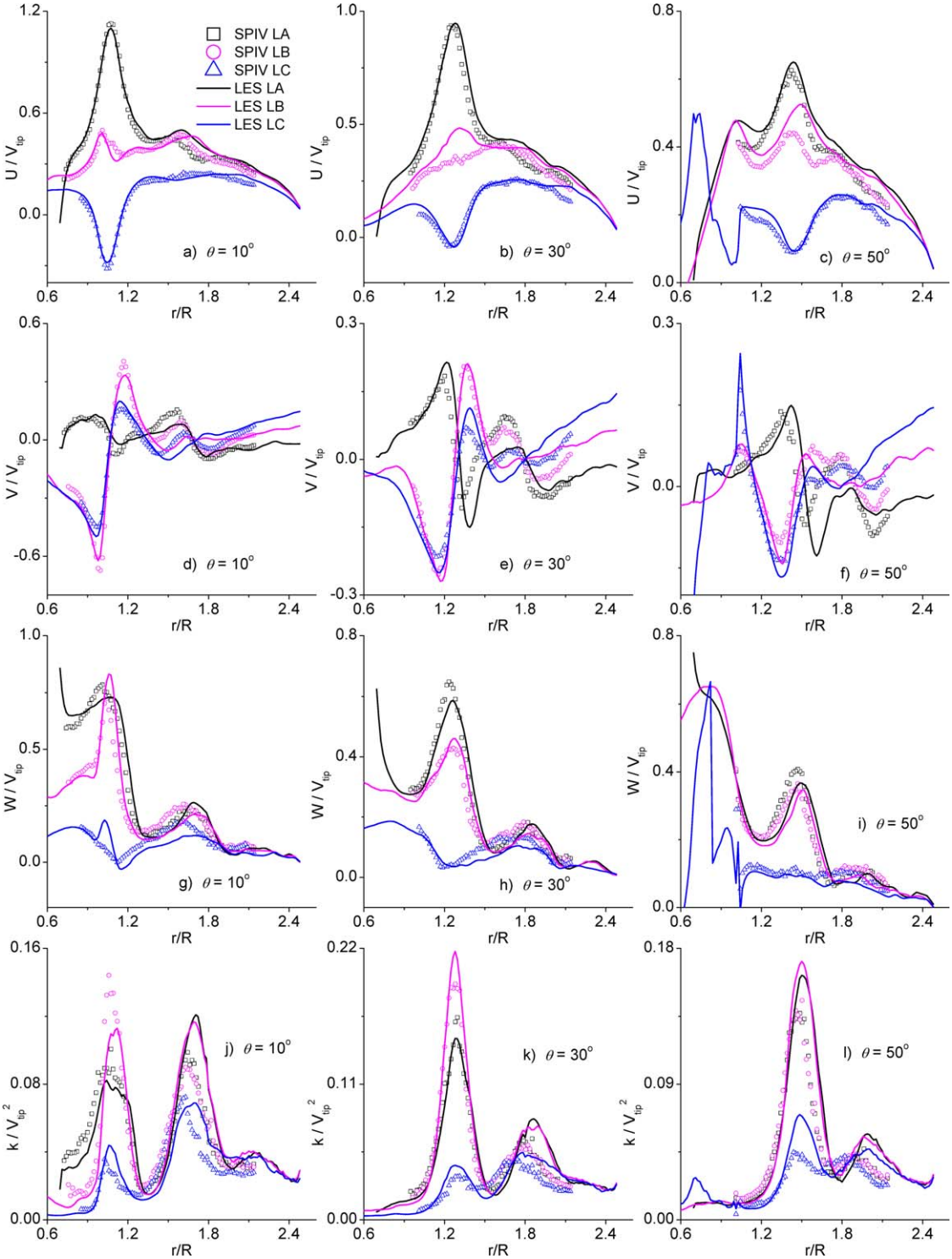

Figure 12. Phase-resolved velocity and TKE profiles obtained by SPIV and LES for CD impeller at $\theta = 10^\circ$, 30°, and 50° (LA: $2z/w = 0$; LB: $2z/w = 0.5$; LC: $2z/w = 1.0$).

[Color figure can be viewed in the online issue, which is available at wileyonlinelibrary.com.]

Therefore, grid refinement should cover the entire region affected by trailing vortices, and further investigations need to be conducted on the phase-resolved flow fields of stirred tanks.

Phase-resolved results of HEDT impeller

Figures 13 and 14 show the phase-resolved flow fields of the HEDT impeller obtained by SPIV and LES, respectively, and the agreement between the SPIV experiments and the LES predictions is generally good. In addition to the phase-resolved results of the CD impeller (see Figures 10 and 11) and RTs[12,13] (qualitative experimental and simulated results of Rushton turbines can be easily found in the literature and are not presented here for conciseness), it can be found that a pair of counter-rotating vortices always exists for different streamlined-blade disk turbines, and the regions with high

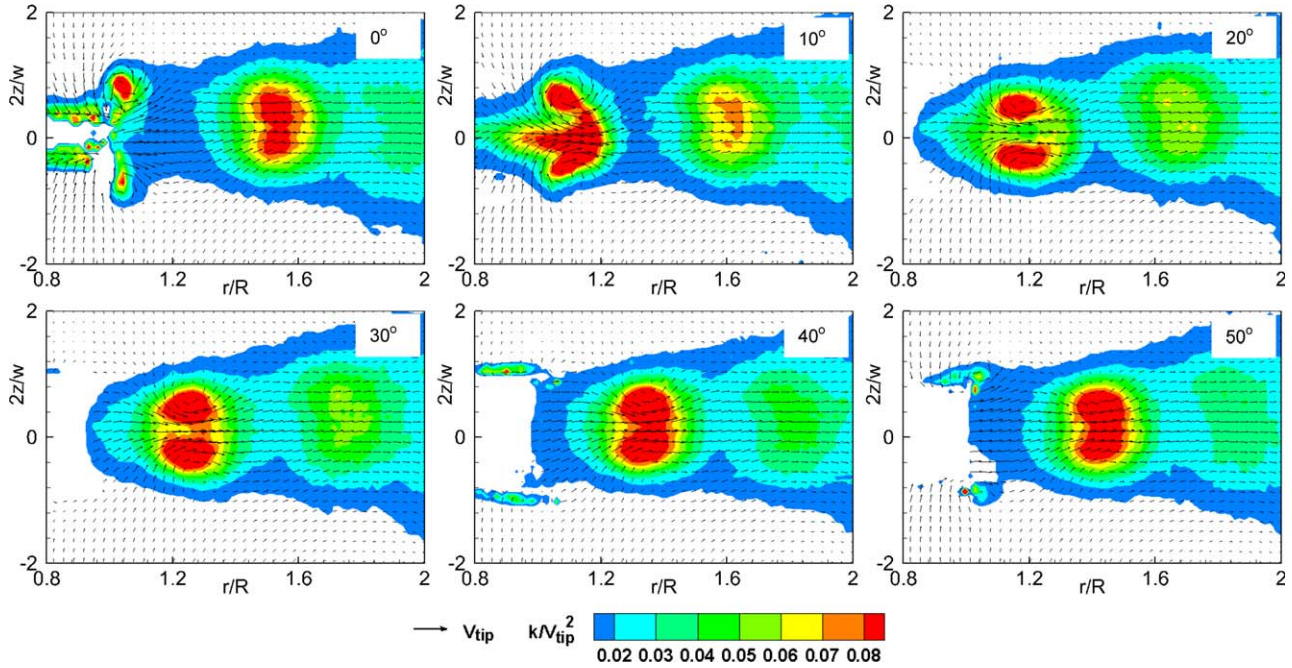

Figure 13. Phase-resolved plots of velocity and TKE fields obtained by SPIV for HEDT impeller at $\theta = 0°$, 10°, 20°, 30°, 40°, and 50°.

[Color figure can be viewed in the online issue, which is available at wileyonlinelibrary.com.]

TKE levels are closely associated with the movements of trailing vortices and extend more than 60° in the tangential direction (see Figures 10 and 13).

Figure 15 compares the velocity and TKE profiles of the HEDT impeller at $\theta = 10°$, 30°, and 50°, and the locations of three horizontal lines are the same as those in Figure 12. The good agreement between the simulated and experimental profiles further confirms the advantage of LES in predicting the complex flows in stirred tanks. However, some discrepancies between the LES and SPIV results can be observed in Figures 13–15, because the simulated results were obtained by using LES with medium resolution hybrid grid. Another possible reason for the discrepancies is that the differences between the physical impeller used in our experiments and the impeller model adopted in LES are more pronounced for HEDT, which is more complex than RT and CD. Although considerable effort has been made during the manufacture of the turbine, minor differences in

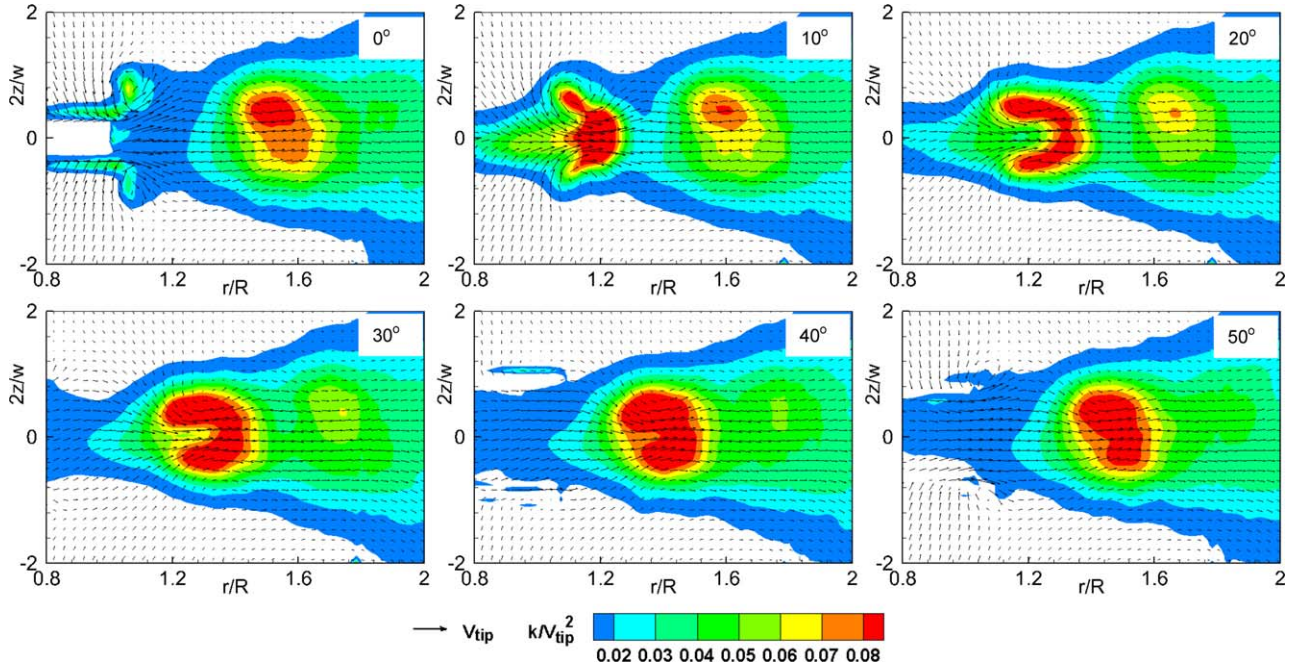

Figure 14. Phase-resolved plots of velocity and TKE fields simulated by LES for HEDT impeller at $\theta = 0°$, 10°, 20°, 30°, 40°, and 50°.

[Color figure can be viewed in the online issue, which is available at wileyonlinelibrary.com.]

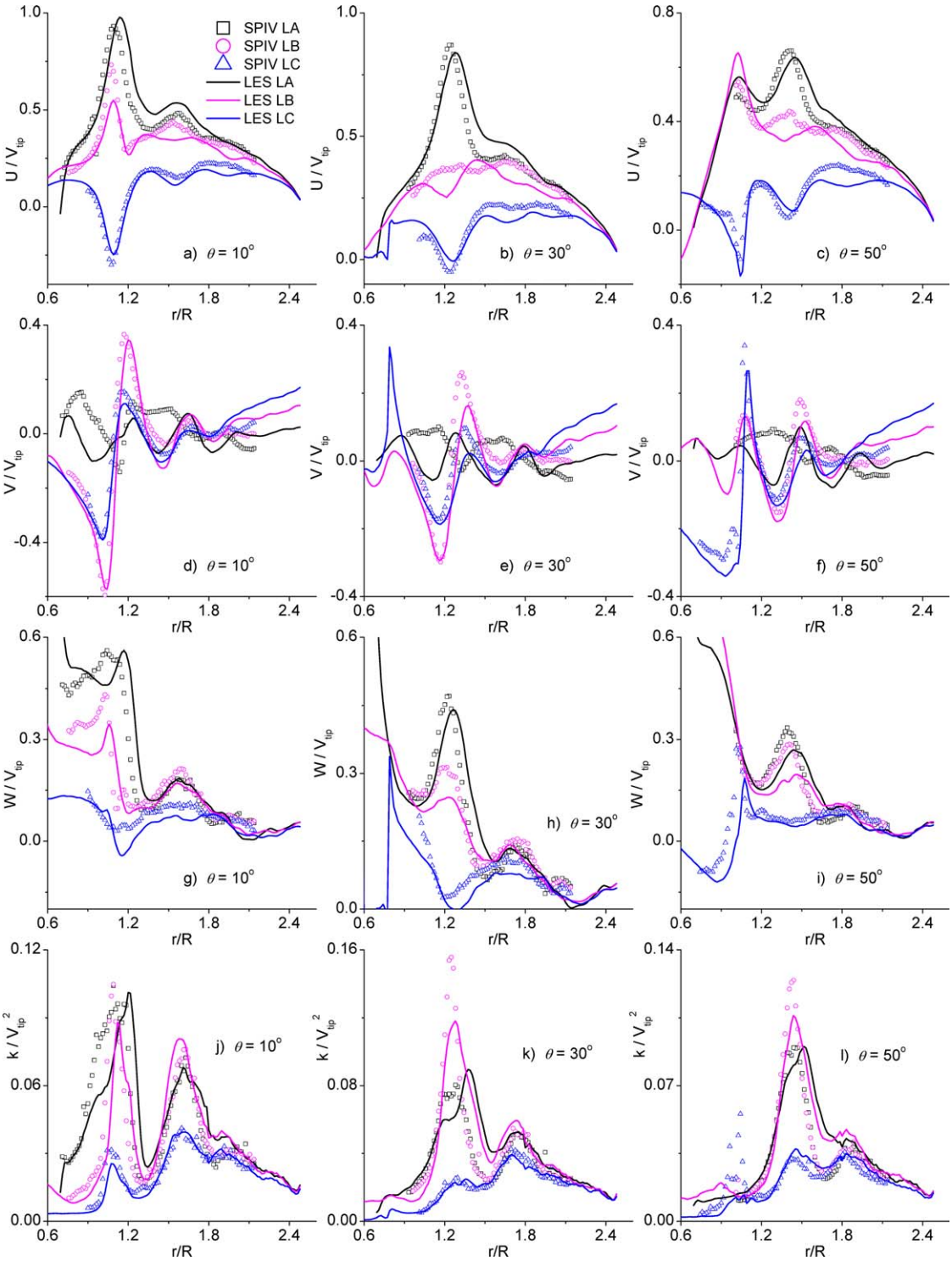

Figure 15. Phase-resolved velocity and TKE profiles obtained by SPIV and LES for HEDT impeller at $\theta = 10^\circ$, 30°, and 50° (LA: $2z/w = 0$; LB: $2z/w = 0.5$; LC: $2z/w = 1.0$).

[Color figure can be viewed in the online issue, which is available at wileyonlinelibrary.com.]

shape are still unavoidable, especially for such pilot-scale experiments.

The above detailed comparisons of the flow fields of RT, CD, and HEDT impellers show that LES is an effective approach for the design and optimization of stirred tanks, and this method is also computationally affordable for pilot-scale stirred tanks. Further investigations, such as mesh resolution and numerical methods, should be conducted on the phase-resolved flow fields. For cases in which experiments are very expensive or difficult to conduct, the LES method can be considered as a good and reliable alternative.

Characteristics of trailing vortices

In order to illustrate the generation and evolution of trailing vortices, planes near the measured blade at $\theta = 0^\circ$, 6°, and 12° are used for the RT impeller with flat blades (Figure

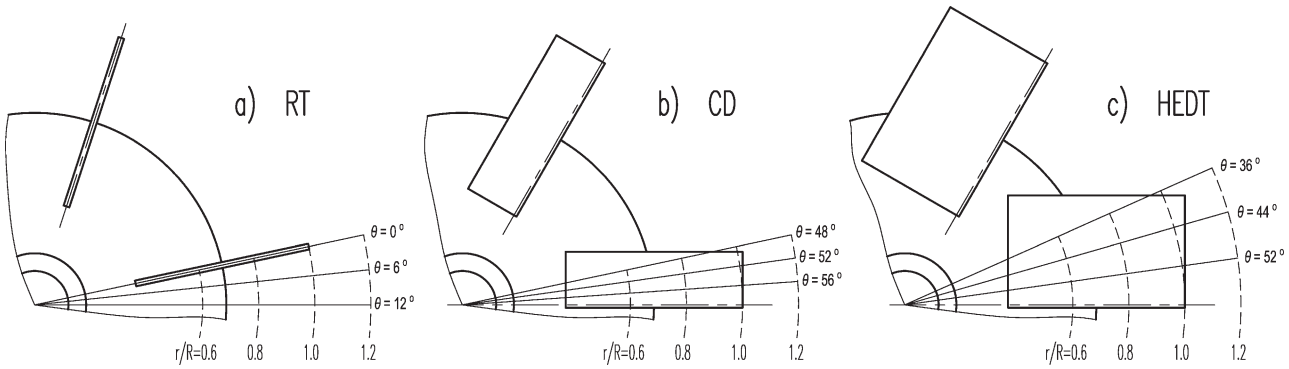

Figure 16. Measurement planes used to illustrate trailing vortices near blades of RT, CD, and HEDT impellers.

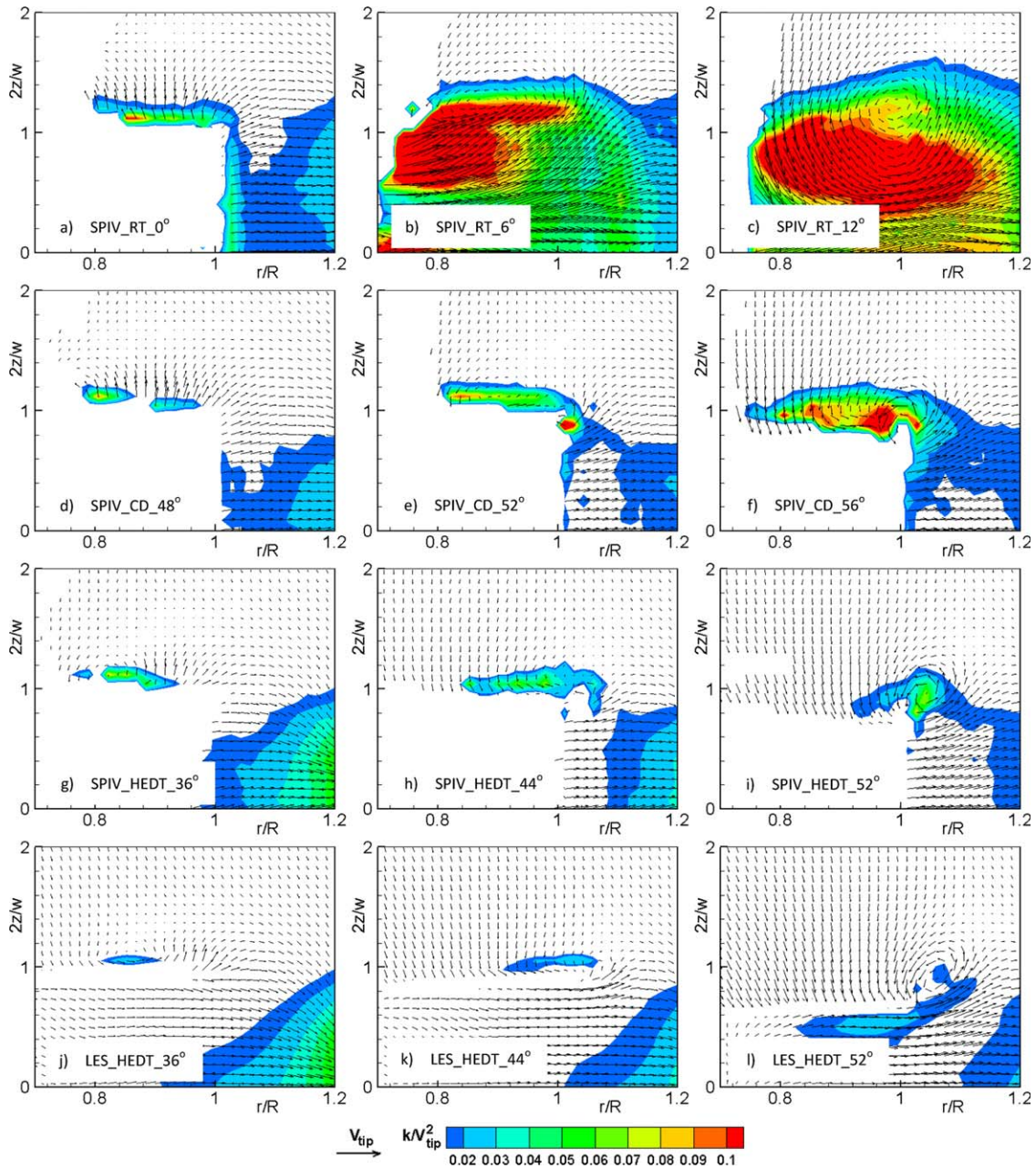

Figure 17. Characteristics of trailing vortices and TKE near blades of RT, CD, and HEDT impellers.

[Color figure can be viewed in the online issue, which is available at wileyonlinelibrary.com.]

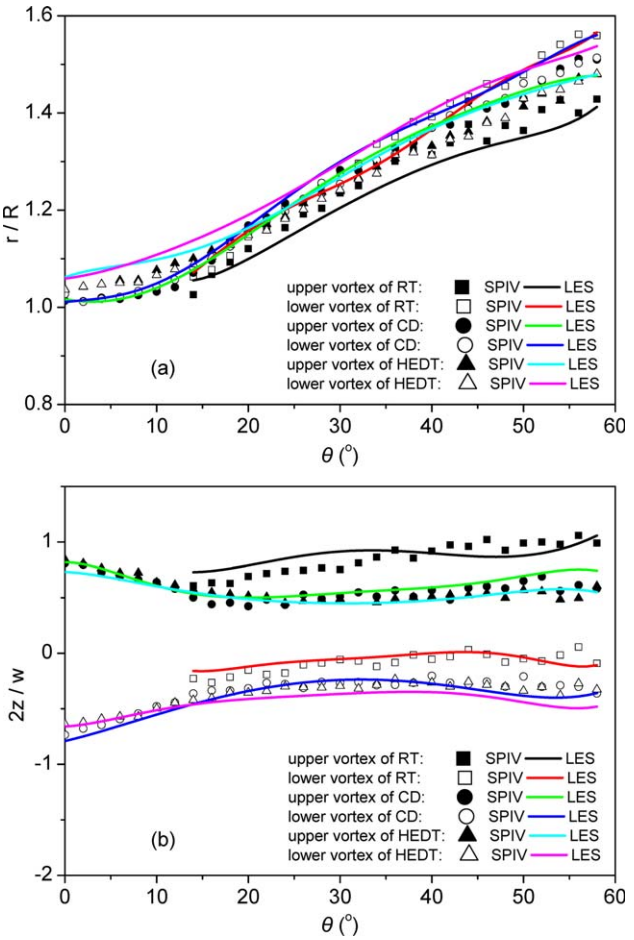

Figure 18. (a) Radial and (b) axial displacements of trailing vortex cores of RT, CD, and HEDT impellers.

[Color figure can be viewed in the online issue, which is available at wileyonlinelibrary.com.]

16a), and planes across the trailing blades are used for the CD and the HEDT impeller, as shown in Figures 16b,c, respectively. The plots of velocity and TKE for the above planes are shown in Figure 17, where only the flow fields near the upper trailing vortices of the blades are shown for clarity. The blank regions in Figures 17a–i were caused by both the projection of the blades and the laser reflection near those blades, although the reflection has been minimized in our experiments.

For the RT impeller, an originally elliptical vortex is generated and shed from the upper edge of the blade, as shown in Figure 17b. This vortex is gradually becoming circular and moves to the upper-right corner of the blade at $\theta = 12^\circ$ (see Figure 17c), because of the rotation of the blade. When the blades are streamlined, the vortices induced by flow separations can be clearly observed near the upper edges of the blades, as shown in Figures 17d (around $r/R = 0.72$) and g (around $r/R = 0.84$). These vortices are strengthened by the sweep of the blades of the CD impeller and are about elliptical in shape at $\theta = 52^\circ$ (see Figure 17e). However, the vortices are weakened behind the blades of the HEDT impeller (see Figure 17h), because the attachment of the vortices may be enforced by the streamlined blades of the HEDT impeller. Clear circular vortices are finally formed in the vicinity of the side edges of the curved-blades (see Figures 17f, i), whether the vortices induced by the upper edges are weakened or not. The weakened trailing vortices behind the streamlined blades can decrease the area of the regions with low pressure and enhance the performance of gas dispersion of such impellers.

The contours in Figure 17 reveal that trailing vortices are the origin of the regions with high TKE levels, and the shedding, growth, and evolution of these vortices lead to the mechanical energy transport from the impeller to the bulk of the tank.

Near the blades of the RT, CD, and HEDT impellers, the vortex characteristics and TKE distributions predicted by LES (Figures17j–l) are in excellent agreement with the experimental data (Figures 17g–i), but only the results for the HEDT impeller are listed in the present work for conciseness.

Jeong and Hussain's[50] technique was used to identify the cores of the above-mentioned trailing vortices after their generations, and the radial and axial displacements of the vortex cores are shown in Figure 18. The upper and the lower vortex core of the RT impeller have apparently different radial displacements, and the lower one moves faster than the upper one in the radial direction (Figure 18a). The two vortex cores of the RT impeller move slightly upward in the axial direction (Figure 18b). This upward movement causes the upward characteristics of the phase-averaged discharge stream of the RT impeller, as shown in Figure 4. For the two curved-blade impellers (CD and HEDT), the upper and the lower vortex core are almost symmetric along the plane $2z/w = 0$ by considering both the radial (Figure 18a) and the axial (Figure 18b) displacement of the vortex cores.

Both the radial and the axial trajectory of the vortex cores predicted by LES with DSL SGS models are in good agreement with the corresponding experimental results. Some discrepancies between the LES and SPIV data can also be found in Figure 18 and need to be reduced in the future.

Conclusions

Both phase-averaged and phase-resolved velocity and TKE fields in stirred tanks with RT and curved-blade turbines (CD and HEDT) were measured by using a stereoscopic PIV system with high resolution, and the generation and evolution of the trailing vortices near the blades of the three turbines were also highly resolved. Flow separations first occur at the upper and the lower edges of all turbines, but the vortices induced by such separations will soon be attached to the trailing faces of the blades when the blades are streamlined. A pair of counter-rotating vortices is generated behind each blade near the tip of the blades for all three turbines. Vortices provide a source of turbulence, and the regions with high TKE levels are transported by the movement of the trailing vortices, leading to the transport of mechanical energy from the impeller to the bulk of the tank.

For baffled stirred tanks operating under fully turbulent conditions, the Reynolds number has no influence on the normalized phase-resolved and phase-averaged velocity and TKE distributions. The differences between the normalized TKE distributions for RT, CD, and HEDT impellers at the same Reynolds number are due to the different power inputs; however, the absolute TKE fields are similar for these impellers given at the same power input. Detailed phase-resolved velocity and TKE profiles are quantitatively provided to enrich the data bases used to verify numerical methods, and

other experimental data (not listed for conciseness) are also available upon request.

The simulated results obtained by using LES with four different subgrid scale models were assessed based on the phase-resolved flow field of RT impeller. The DKE model gives the maximum averaged standard deviations for both mean velocity components and TKE. The WALE model is very promising but has obvious oscillations and needs to be further verified. The SSL model presents slightly better results than the DSL model from the viewpoint of averaged standard deviation, but the difference is not significant. Mesh refinement is beneficial to the present LESs, and the hybrid grid with medium mesh resolution can be considered as a compromise between computational effort and numerical accuracy. The phase-resolved LES results of all three turbines are in excellent agreement with the corresponding experimental data, and the trailing vortex characteristics near the blades are accurately predicted. Therefore, LES method is an effective tool in predicting the complex flow fields in stirred tanks, and it is also computationally affordable for the application of pilot-scale stirred tanks.

Acknowledgments

The authors gratefully acknowledge the financial support from the National Natural Science Foundation of China (Nos. 20990224, 21121064, 21206002).

Notation

Roman characters

C_s = Smagorinsky coefficient
d = distance to closest wall, m
D = diameter of impeller, m
H = height of liquid in tank, m
k = turbulent kinetic energy, $m^2\ s^{-2}$
k_{sgs} = subgrid scale turbulent kinetic energy, $m^2\ s^{-2}$
N = rotational speed, s^{-1}
p = pressure, Pa
P = power consumption, W
r = radial coordinate, m
R = radius of impeller, m
Re = Reynolds number
S_{ij} = strain rate tensor, s^{-1}
t = time, s
T = diameter of stirred tank, m
u_i = instantaneous velocity in ith direction, $m\ s^{-1}$
U, V, W = mean radial, axial, and tangential velocity, respectively, $m\ s^{-1}$
V_{tip} = tip velocity of impeller, $m\ s^{-1}$
w = width of blade, m
x_i = spatial component in ith direction, m
z = axial coordinate, m

Greek letters

Δ = filter width, m
δ_{ij} = Kronecker's delta
θ = angle between current blade and measurement plane, rad
ν = kinematic viscosity, $m^2\ s^{-1}$
ν_t = eddy viscosity, $m^2\ s^{-1}$
τ_{ij} = subgrid scale stress tensor in grid filter, $m^2\ s^{-2}$

Literature Cited

1. Vasconcelos JMT, Orvalho SCP, Rodrigues AMAF, Alves SS. Effect of blade shape on the performance of six-bladed disk turbine impellers. *Ind Eng Chem Res*. 2000;39:203–213.
2. Smith JM, Gao Z. Power demand of gas dispersing impellers under high load conditions. *Trans Inst Chem Eng*. 2001;79A:575–580.
3. Paul EL, Atiemo-Obeng VA, Kresta SM. Handbook of Industrial Mixing: Science and Practice. Hoboken, NJ: John Wiley & Sons, Inc., 2004.
4. Bao Y, Gao Z, Li Z, Bai D, Smith JM, Thorpe RB. Solid suspension in a boiling stirred tank with radial flow turbines. *Ind Eng Chem Res*. 2008;47:2420–2427.
5. Revstedt J, Fuchs L, Kovacs T, Tragardh C. Influence of impeller type on the flow structure in a stirred reactor. *AIChE J*. 2000;46:2373–2382.
6. Revstedt J, Fuchs L. Large eddy simulation of flow in stirred vessels. *Chem Eng Technol*. 2002;25:443–446.
7. Zhao J, Gao Z, Bao Y. Effects of the blade shape on the trailing vortices in liquid flow generated by disc turbines. *Chin J Chem Eng*. 2011;19:232–242.
8. Yianneskis M, Popiolek Z, Whitelaw JH. An experimental study of the steady and unsteady flow characteristics of stirred reactors. *J Fluid Mech*. 1987;175:537–555.
9. Wu H, Patterson GK. Laser-Doppler measurements of turbulent-flow parameters in a stirred mixer. *Chem Eng Sci*. 1989;44:2207–2221.
10. Zhou G, Kresta SM. Impact of tank geometry on the maximum turbulence energy dissipation rate for impellers. *AIChE J*. 1996;42:2476–2490.
11. Lee KC, Yianneskis M. Turbulence properties of the impeller stream of a Rushton turbine. *AIChE J*. 1998;44:13–24.
12. Sharp KV, Adrian RJ. PIV study of small-scale flow structure around a Rushton turbine. *AIChE J*. 2001;47:766–778.
13. Escudie R, Line A. Experimental analysis of hydrodynamics in a radially agitated tank. *AIChE J*. 2003;49:585–603.
14. Yoon HS, Hill DF, Balachandar S, Adrian RJ, Ha MY. Reynolds number scaling of flow in a Rushton turbine stirred tank. Part I—mean flow, circular jet and tip vortex scaling. *Chem Eng Sci*. 2005;60:3169–3183.
15. Unadkat H, Rielly CD, Nagy ZK. PIV study of the flow field generated by a sawtooth impeller. *Chem Eng Sci*. 2011;66:5374–5387.
16. Khan FR, Rielly CD, Brown DAR. Angle-resolved stereo-PIV measurements close to a down-pumping pitched-blade turbine. *Chem Eng Sci*. 2006;61:2799–2806.
17. Joshi JB, Nere NK, Rane CV, Murthy BN, Mathpati CS, Patwardhan AW, Ranade VV. CFD simulation of stirred tanks: comparison of turbulence models. Part I: radial flow impellers. *Can J Chem Eng*. 2011;89:23–82.
18. Joshi JB, Nere NK, Rane CV, Murthy BN, Mathpati CS, Patwardhan AW, Ranade VV. CFD simulation of stirred tanks: comparison of turbulence models. Part II: axial flow impellers, multiple impellers and multiphase dispersions. *Can J Chem Eng*. 2011;89:754–816.
19. Eggels JGM. Direct and large-eddy simulation of turbulent fluid flow using the lattice-Boltzmann scheme. *Int J Heat Fluid Flow*. 1996;17:307–323.
20. Derksen J, van den Akker HEA. Large eddy simulations on the flow driven by a Rushton turbine. *AIChE J*. 1999;45:209–221.
21. Derksen J. Assessment of large eddy simulations for agitated flows. *Trans Inst Chem Eng*. 2001;79A:824–830.
22. Lu ZY, Liao Y, Qian DY, McLaughlin JB, Derksen JJ, Kontomaris K. Large eddy simulations of a stirred tank using the lattice Boltzmann method on a nonuniform grid. *J Comput Phys*. 2002;181:675–704.
23. Hartmann H, Derksen JJ, Montavon C, Pearson J, Hamill IS, van den Akker HEA. Assessment of large eddy and RANS stirred tank simulations by means of LDA. *Chem Eng Sci*. 2004;59:2419–2432.
24. Revstedt J, Fuchs L, Tragardh C. Large eddy simulations of the turbulent flow in a stirred reactor. *Chem Eng Sci*. 1998;53:4041–4053.
25. Zhang YH, Yang C, Mao ZS. Large eddy simulation of liquid flow in a stirred tank with improved inner-outer iterative algorithm. *Chin J Chem Eng*. 2006;14:321–329.
26. Yoon HS, Balachandar S, Ha MY, Kar K. Large eddy simulation of flow in a stirred tank. *ASME J Fluids Eng*. 2003;125:486–499.
27. Yoon HS, Balachandar S, Ha MY. Large eddy simulation of flow in an unbaffled stirred tank for different Reynolds numbers. *Phys Fluids*. 2009;21:085102.
28. Roussinova V, Kresta SM, Weetman R. Low frequency macroinstabilities in a stirred tank: scale-up and prediction based on large eddy simulation. *Chem Eng Sci*. 2003;58:2297–2311.
29. Yeoh SL, Papadakis G, Lee KC, Yianneskis M. Large eddy simulation of turbulent flow in a Rushton impeller stirred reactor with

sliding-deforming mesh methodology. *Chem Eng Technol*. 2004;27:257–263.
30. Yeoh SL, Papadakis G, Yianneskis M. Numerical simulation of turbulent flow characteristics in a stirred vessel using the LES and RANS approaches with the sliding/deforming mesh methodology. *Chem Eng Res Des*. 2004;82:834–848.
31. Bakker A, Oshinowo LM. Modelling of turbulence in stirred vessels using large eddy simulation. *Chem Eng Res Des*. 2004;82:1169–1178.
32. Alcamo R, Micale G, Grisafi F, Brucato A, Ciofalo M. Large-eddy simulation of turbulent flow in an unbaffled stirred tank driven by a Rushton turbine. *Chem Eng Sci*. 2005;60:2303–2316.
33. Tyagi M, Roy S, Harvey AD III, Acharya S. Simulation of laminar and turbulent impeller stirred tanks using immersed boundary method and large eddy simulation technique in multi-block curvilinear geometries. *Chem Eng Sci*. 2007;62:1351–1363.
34. Jahoda M, Mostek M, Kukukova A, Machon V. CFD modelling of liquid homogenization in stirred tanks with one and two impellers using large eddy simulation. *Chem Eng Res Des*. 2007;85:616–625.
35. Murthy BN, Joshi JB. Assessment of standard k-ε, RSM and LES turbulence models in a baffled stirred vessel agitated by various impeller designs. *Chem Eng Sci*. 2008;63:5468–5495.
36. Delafosse A, Line A, Morchain J, Guiraud P. LES and URANS simulations of hydrodynamics in mixing tank: comparison to PIV experiments. *Chem Eng Res Des*. 2008;86:1322–1330.
37. Lamarque N, Zoppe B, Lebaigue O, Dolias Y, Bertrand M, Ducros F. Large-eddy simulation of the turbulent free-surface flow in an unbaffled stirred tank reactor. *Chem Eng Sci*. 2010;65:4307–4322.
38. Zadghaffari R, Moghaddas JS, Revstedt J. Large-eddy simulation of turbulent flow in a stirred tank driven by a Rushton turbine. *Comput Fluids*. 2010;39:1183–1190.
39. Li Z, Gao Z, Smith JM, Thorpe RB. Large eddy simulation of flow fields in vessels stirred by dual Rushton impeller agitators. *J Chem Eng Jpn*. 2007;40:684–691.
40. Li Z, Bao Y, Gao Z. PIV experiments and large eddy simulations of single-loop flow fields in Rushton turbine stirred tanks. *Chem Eng Sci*. 2011;66:1219–1231.
41. Li Z, Hu M, Bao Y, Gao Z. Particle image velocimetry experiments and large eddy simulations of merging flow characteristics in dual Rushton turbine stirred tanks. *Ind Eng Chem Res*. 2012;51:2438–2450.
42. Wu B. Large eddy simulation of mechanical mixing in anaerobic digesters. *Biotechnol Bioeng*. 2012;109:804–812.
43. Lu Y, Shen GX. Three-dimensional flow structures and evolution of the leading-edge vortices on a flapping wing. *J Exp Biol*. 2008;211:1221–1230.
44. Smagorinsky J. General circulation experiments with the primitive equations. *I. The basic experiment*. *Mon Weather Rev*. 1963;91:99–164.
45. ANSYS Inc. ANSYS FLUENT Theory Guide. Canonsburg, PA: ANSYS Inc., 2010.
46. Germano M, Piomelli U, Moin P, Cabot WH. A dynamic subgrid-scale eddy viscosity model. *Phys Fluids A*. 1991;3:1760–1765.
47. Lilly DK. A proposed modification of the Germano subgrid-scale closure method. *Phys Fluids A*. 1992;4:633–635.
48. Kim WW, Menon S. Application of the localized dynamic subgrid-scale model to turbulent wall-bounded flows. Technical report AIAA-97-0210. Reno, NV: AIAA Inc., 1997.
49. Nicoud F, Ducros F. Subgrid-scale stress modeling based on the square of the velocity gradient tensor. *Flow Turbul Combust*. 1999;62:183–200.
50. Jeong J, Hussain F. On the identification of a vortex. *J Fluid Mech*. 1995;285:69–94.

Manuscript received Nov. 7, 2012, and revision received Mar. 1, 2013.